Chemical Science

ROYAL SOCIETY OF CHEMISTRY

EDGE ARTICLE

View Article Online
View Journal

Check for updates

Cite this: DOI: 10.1039/d5sc09348a

All publication charges for this article have been paid for by the Royal Society of Chemistry

Received 29th November 2025
Accepted 19th May 2026

DOI: 10.1039/d5sc09348a

rsc.li/chemical-science

Noble-metal-free π-stacked metal–organic nanosheets featuring unidirectional electron transport channels for highly efficient electrocatalytic CO_2 reduction

Qiuping Xie,[a] Yunxiang He,[ab] Qinling Liu,[ac] Siqi Deng,[a] Xiaoling Wang,[ab] Wen Liao,[d] Gonghua Hong,*[ab] Ian Manners †[e] and Junling Guo *[abfg]

Two-dimensional (2D) electrocatalysts are widely explored for electrocatalytic CO_2 reduction, yet disordered electron transport within these catalysts often limits performance due to elongated electron pathways and poor accessibility to catalytic sites. Here, we report a noble-metal-free 2D metal–organic electrocatalyst (MPhene) featuring unique unidirectional electron transport channels formed *via* long-range π–π stacking of natural phenolic bio-ligands. These ordered molecular structures facilitate highly efficient electron transport to catalytic bismuth (Bi^{III})-coordinated centers, enabling highly selective CO_2 reduction to formic acid (HCOOH) with >90% selectivity across a broad potential window (−0.7 to −1.1 V *vs.* the reversible hydrogen electrode). Notably, MPhene achieves a peak partial current density of 115.5 mA cm^{-2} for HCOOH production, representing record-high electrocatalytic activity and significantly surpassing the performance of all previously reported advanced noble-metal-free 2D electrocatalysts in neutral electrolytes. *In situ* Raman spectroscopy and theoretical calculations reveal the critical role of unique unidirectional electron transport channels in enhancing catalytic performance. This work introduces a novel supramolecular design strategy for controlling electron transport in noble-metal-free 2D electrocatalysts, offering new opportunities in photocatalysis, photoelectronics, and CO_2 reduction technologies.

Introduction

The overconsumption of fossil fuels and the sharp rise in atmospheric CO_2 have raised urgent concerns over energy depletion and triggered escalating environmental crises such as global warming and climate instability.[1–4] Electrocatalytic CO_2 reduction driven by renewable electricity provides a sustainable and efficient route to convert abundant CO_2 into value-added products, thereby contributing to both carbon mitigation and the clean energy transition.[5–14] Within diverse electrocatalyst architectures, two-dimensional (2D) materials have garnered significant attention due to their high surface area and richly exposed active sites, which collectively promote efficient CO_2 adsorption and facilitate electron transfer.[15] Among them, graphene stands out for its ultrahigh electrical conductivity, which arises from its extended in-plane π-conjugation and crystalline order, enabling delocalized charge transport across the 2D lattice. However, despite its superior conductivity, graphene and similar inorganic 2D materials (transition metal dichalcogenides, hexagonal boron nitride, *etc.*) often suffer from limited tunability and a lack of precise control over electron pathways. More importantly, the absence of directional, in-plane charge-transport pathways often leads to resistive losses and sub-optimal site accessibility in the CO_2 reduction reaction (CO_2RR).[16–18]

A lack of directionality in charge migration constitutes not merely a structural imperfection but a fundamental kinetic constraint that limits the efficiency of electrocatalysis by disrupting the coherent delivery of electrons. Prolonged electron

---

[a] *BMI Center for Biomass Materials and Nanointerfaces, College of Biomass Science and Engineering, Sichuan University, Chengdu, Sichuan 610065, China. E-mail: gonghua.hong@scu.edu.cn; junling.guo@scu.edu.cn*

[b] *National Engineering Laboratory for Clean Technology of Leather Manufacture, Ministry of Education Key Laboratory of Leather Chemistry and Engineering, Sichuan University, Chengdu, Sichuan 610065, China*

[c] *Tea Refining and Innovation Key Laboratory of Sichuan Province, College of Horticulture, Sichuan Agricultural University, Chengdu, Sichuan 611130, China*

[d] *State Key Laboratory of Oral Diseases & National Clinical Research Center for Oral Diseases, West China Hospital of Stomatology, Sichuan University, Chengdu, Sichuan 610041, PR China*

[e] *Department of Chemistry, University of Victoria, Victoria, BC V8W 3V6, Canada*

[f] *State Key Laboratory of Polymer Materials Engineering, Sichuan University, Chengdu, Sichuan 610065, China*

[g] *Bioproducts Institute, Department of Chemical and Biological Engineering, The University of British Columbia, Vancouver, BC V6T 1Z4, Canada. E-mail: junling.guo@ubc.ca*

† Deceased December 3rd, 2023.

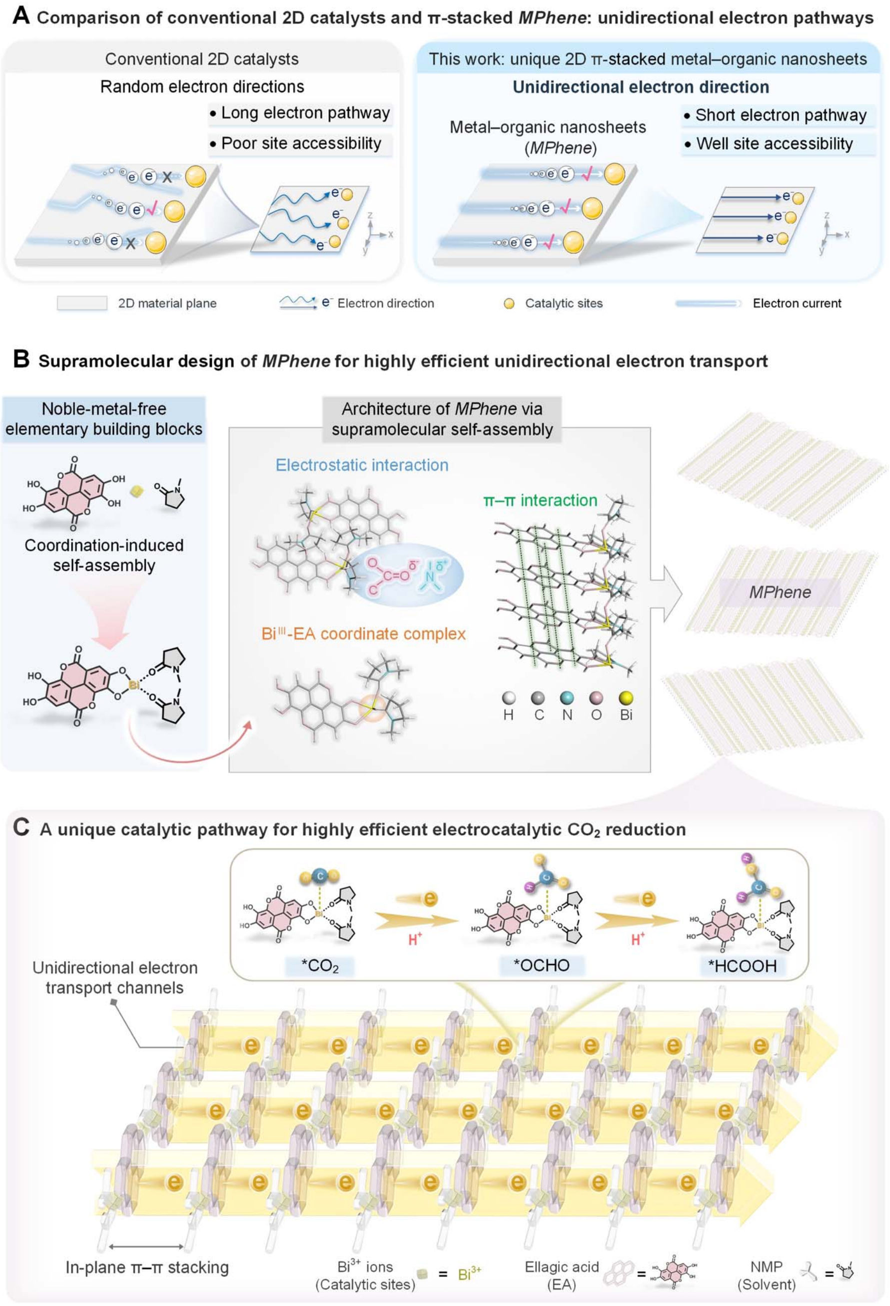

Fig. 1 Electrocatalytic CO_2 reduction by metal–organic nanosheets with unique unidirectional electron transport channels. (A) Comparative illustration of electron transport pathways in conventional 2D electrocatalysts (left) *versus* 2D π-stacked metal–organic nanosheets (MPhene, right). The conventional 2D electrocatalysts exhibit randomized electron directions, leading to extended transport pathways and limited catalytic site accessibility. In contrast, the MPhene nanosheets demonstrate unique unidirectional electron flow, enabling highly efficient electron transport and optimal accessibility of active sites. (B) Molecular architecture of MPhene nanosheets formed through coordinated assembly of the phenolic ligand, ellagic acid (EA, found in fruits, vegetables, and tree bark), with bismuth ions (Bi^{3+}) and *N*-methyl-2-pyrrolidone (NMP). Further supramolecular organization *via* π–π stacking yields well-defined 2D nanosheets with aligned electron transport channels. (C) Mechanistic illustration of electrocatalytic CO_2 reduction on MPhene nanosheets. The unique long-range π–π stacking within MPhene nanosheets enables highly efficient electron transport to Bi^{III} active centers, promoting stepwise CO_2 reduction and hydrogenation pathways toward highly selective HCOOH production.

migration pathways exacerbate energy losses through phonon scattering,[19–21] thereby diminishing the redox-driving capability at catalytic interfaces (Fig. 1A). Although strategies such as heterojunction engineering have been employed to enhance charge transport, the stochastic nature of electron motion at the nanoscale continues to hinder the realization of efficient and unidirectional charge flow.[22] To overcome these limitations, organic 2D materials, including conjugated polymers, covalent organic frameworks (COFs), and metal–organic layers (MOLs), have emerged as chemically versatile platforms offering modular design capabilities at the molecular level. The structural tunability of these frameworks enables the integration of diverse functional units and the fine-tuning of electronic environments. However, their practical application in electrocatalysis remains limited by intrinsically low charge mobility, primarily due to weak inter-unit electronic coupling and the lack of extended conductive pathways.[23]

π–π stacking provides a strong and highly directional intermolecular interaction that facilitates charge delocalization along defined spatial axes. It is commonly exploited in organic electronic materials and supramolecular assemblies to enhance charge transport, and is observed in systems such as metal–organic frameworks (MOFs) and perylene imide derivatives.[24,25] These face-to-face stacked architectures support long-range exciton and electron transport, analogous to ion migration through nanoscale ion channels in nature. However, traditional MOFs typically adopt three-dimensional (3D) frameworks with out-of-plane π stacking, while perylene-based assemblies often form one-dimensional (1D) fibrous morphologies, both of which fall short of providing in-plane electronic coherence required for efficient 2D catalysis. In contrast, in-plane π stacking offers a promising route to establish aligned charge transport networks within organic 2D frameworks. While certain materials, such as MOLs and poly(phenylene vinylene) (PPV), display in-plane π-stacking motifs, they often lack long-range order or adopt parallel-displaced configurations, which limit their effectiveness in establishing contiguous in-plane π-stacks that act as preferential charge-transport pathways.[26,27] Therefore, the rational construction of 2D organic materials featuring long-range, in-plane π-stacking architectures remains a major challenge with great promise for addressing unidirectional transport bottlenecks.

Herein, we report a noble-metal-free 2D electrocatalyst (MPhene) featuring unique in-plane π-stacking structures aligned parallel to catalytic bismuth (Bi^{III})-coordinated centers (Fig. 1B). These nanosheets are constructed from plant-derived polyphenols enriched with catechol and galloyl moieties, which engage in a spectrum of covalent and non-covalent interactions, including metal coordination, hydrogen bonding, and π–π stacking.[28–40] The delicate balance between thermodynamic and kinetic parameters during assembly enables fine-tuning of both the structural architecture and electronic characteristics.[41,42] Critically, the formation of unique in-plane π-stacking networks within the 2D supramolecular phenolic framework establishes continuous electron channels that promote highly efficient unidirectional charge transport toward Bi^{III} active sites (Fig. 1C). Owing to this architecturally coherent charge transport pathway, the MPhene nanosheets efficiently catalyze the reduction of CO_2 to formic acid (HCOOH), achieving over 90% selectivity across a broad potential window (−0.7 to −1.1 V *vs.* the reversible hydrogen electrode, RHE). Remarkably, the partial current density of HCOOH reaches 115.5 mA cm^{-2} at −1.1 V *vs.* RHE, representing record-high electrocatalytic activity and significantly surpassing the performance of all previously reported advanced noble-metal-free 2D electrocatalysts in neutral electrolytes.[43–53] Importantly, this noble-metal-free system exemplifies how a molecular-level engineering paradigm can achieve superior CO_2 conversion while maintaining sustainability and scalability, circumventing the need for noble-metal components. This work demonstrates a novel strategy for engineering unique unidirectional electron transport channels in 2D electrocatalysts, paving new paths for sustainable energy conversion and carbon management technologies.

Results and discussion

Synthesis and characterization of MPhene

MPhene nanosheets were synthesized *via* ultrasonic exfoliation of our previously reported Bi-EA mesocrystals (referred to here as MPhene precursors), which possess quaternary ordered architectures assembled through synergistic molecular interactions across multiple length scales under spatiotemporal regulation.[31] Scanning electron microscopy (SEM) revealed stacked, plate-like external morphologies of the Bi-EA mesocrystals (Fig. S1), which are consistent with lamellar packing and motivated the subsequent exfoliation study. To obtain nanosheets from the precursor crystals, a liquid-phase exfoliation strategy assisted by ultrasonication was employed, which is a well-established and widely adopted method for the preparation of 2D materials from layered crystalline precursors.[54–56] Specifically, 10 mg of finely ground Bi-EA mesocrystals was dispersed in 1 mL of ethanol and subjected to ultrasonic treatment at 50 W and 40 kHz for 30 minutes. Ethanol was selected as the exfoliation solvent because control experiments showed that solvents with either higher or lower polarity did not yield well-defined nanosheets under otherwise comparable conditions, as evidenced by atomic force microscopy (AFM) analysis (Fig. S2). These results indicate that solvent choice plays a critical role in the exfoliation process, with ethanol providing a suitable balance for achieving effective delamination while preserving nanosheet morphology. In addition, sonication intensity was found to strongly influence the exfoliation outcome. Insufficient power led to incomplete delamination, whereas excessive power caused fragmentation of the nanosheets (Fig. S3). An optimized sonication power of 50 W enabled efficient exfoliation while preserving structural integrity. The resulting colloidal dispersion exhibited a pronounced Tyndall effect, indicating the presence of suspended nanosheets. Dynamic light scattering (DLS) analysis revealed an average hydrodynamic dimension of approximately 2.3 μm (Fig. 2D). Furthermore, electrospray ionization mass spectrometry (ESI-MS) detected no signal corresponding to free ellagic acid ligands or residual *N*-methyl-2-pyrrolidone (NMP), thereby confirming that the molecular framework of MPhene remained intact during ultrasonic treatment (Fig. S4).

To elucidate the morphology of the exfoliated MPhene nanosheets, we performed AFM and scanning transmission electron microscopy (STEM). AFM measurements revealed that the nanosheets had an average thickness of 3.45 nm (Fig. 2A, S5 and Table S1), in agreement with the modeled structure composed of six molecular layers (Fig. S6). To evaluate whether

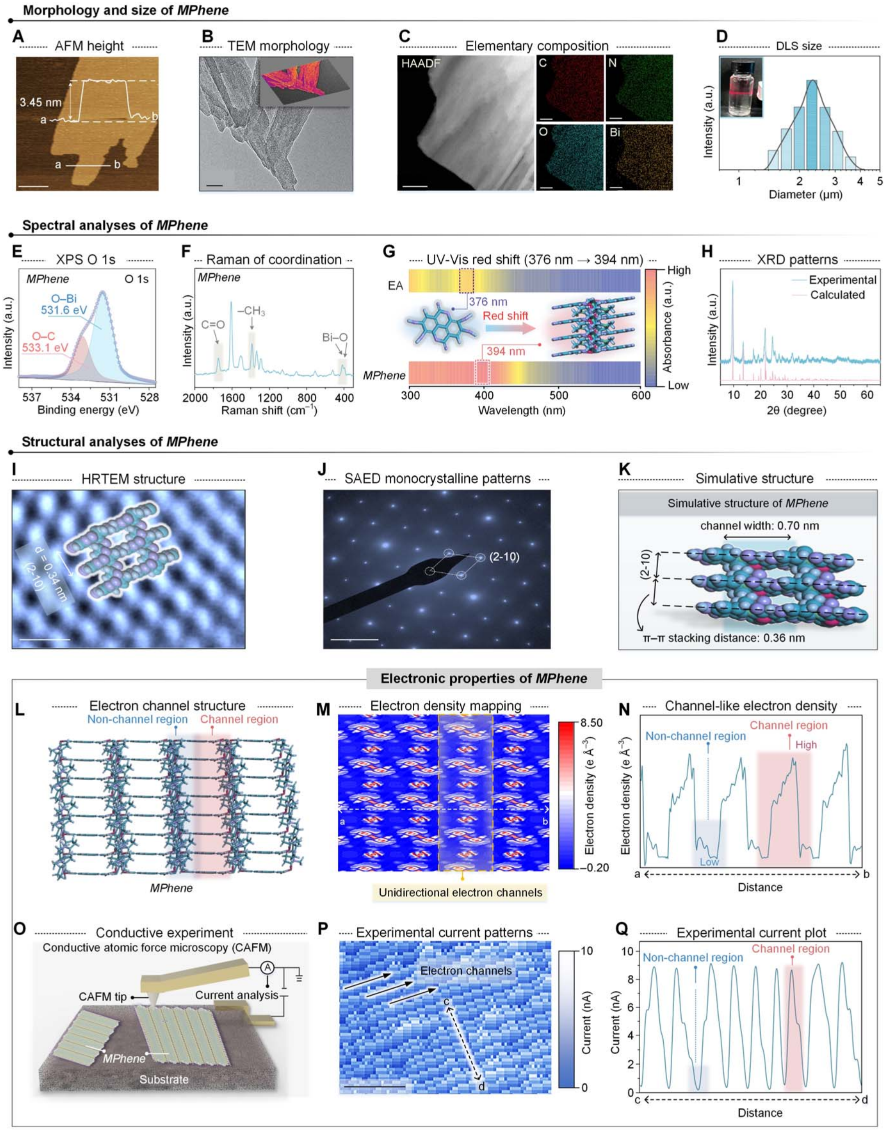

Fig. 2 Morphology and structural analysis of MPhene. (A) AFM image and height profile of MPhene. (B) TEM image and corresponding 3D reconstructed TEM image (inset) of MPhene. (C) HAADF-STEM image (left) and corresponding EDS elemental mapping images (right) of MPhene. (D) Size distribution and digital photograph (inset) of MPhene dispersed in ethanol. (E) High-resolution XPS spectra of O 1s for MPhene. (F) Raman spectrum of MPhene. (G) UV-vis absorption spectra of MPhene and EA molecules. (H) Experimental and calculated PXRD curves of MPhene. (I and J) HRTEM image (I) and the corresponding SAED pattern (J) of MPhene. (K) Theoretical π-stacking structure and parameters of MPhene. (L) Simulated in-plane structure of MPhene. (M and N) In-plane electron density (M) and corresponding detailed electron density profile (N) of MPhene. (O) Schematic illustration of the conductive measurement using CAFM. (P) Experimental current patterns of MPhene acquired using CAFM. (Q) CAFM-derived current profile of MPhene across electron channels. Scale bars are 1 μm (A and B), 500 nm (C), 1 nm (I), 5 1/nm (J), and 100 nm (P).

further thinning could be achieved, exfoliation was performed under increased sonication intensity. However, neither prolonging the sonication time nor increasing the sonication power resulted in the formation of thinner nanosheets. Instead, irregular small particles were observed (Fig. S7), indicating fragmentation of the exfoliated nanosheets under stronger sonication conditions. These results suggest that the exfoliated nanosheets retain structural integrity at a thickness of approximately six molecular layers, whereas stronger sonication induces fragmentation rather than further thinning.[57,58] The bright-field TEM image further confirmed sheet-like structures with lateral sizes exceeding 2.0 μm (Fig. 2B). In addition, elemental mapping using energy-dispersive X-ray spectroscopy (EDS) showed a homogeneous distribution of carbon (C), nitrogen (N), oxygen (O), and bismuth (Bi), corresponding to the incorporated components of ellagic acid (EA), Bi^{3+} ions, and NMP (Fig. 2C).

To gain molecular-level insight into the coordination environment within the MPhene nanosheets, we conducted a comprehensive spectroscopic analysis. X-ray photoelectron spectroscopy (XPS) analysis of the O 1s region showed two distinct peaks: one at 531.6 eV, assigned to Bi–O bonds, and another at 533.1 eV, attributed to C–O bonding from phenolic groups, indicating that Bi^{3+} ions coordinate with the phenolic groups of EA (Fig. 2E).[59] In parallel, ESI-MS analysis of MPhene after acid dissociation revealed a fragment peak at m/z 100.1, corresponding to NMP (Fig. S8). This result suggests that NMP molecules are retained within the structure and likely act as neutral ligands to balance the residual positive charge associated with Bi^{III}-EA coordination complexes. Further structural evidence was obtained from Fourier-transform (FT) Raman spectroscopy, which displayed a distinct vibrational band at 414 cm^{-1} in the fingerprint region, assignable to Bi–O stretching interactions involving NMP (Fig. 2F).[60] Synchrotron X-ray absorption fine structure (XAFS) spectroscopy was employed to elucidate the local coordination environment of Bi in MPhene nanosheets. The extended X-ray absorption fine structure (EXAFS) fitting reveals two Bi–O distances at 2.16 and 2.35 Å, assigned to Bi–O bonds with EA and NMP, respectively (Fig. S9). The corresponding coordination numbers (1.9 and 2.0; Table S2) indicate that each Bi^{3+} center is coordinated by two catecholate oxygen atoms of EA and two carbonyl oxygen atoms of NMP, confirming a predominantly tetracoordinated configuration in the MPhene nanosheets. Collectively, these results substantiate the formation of a ternary coordination complex composed of Bi^{III}, EA, and NMP as the building unit of the nanosheets. The assembly of these units into extended 2D sheets is further stabilized by π–π stacking interactions between EA ligands. Supporting this, ultraviolet-visible (UV-vis) absorption spectroscopy revealed a redshift in the absorption maximum from 376 nm in free EA ligands to 394 nm in MPhene nanosheets, indicative of enhanced π-conjugation through face-to-face aromatic stacking (Fig. 2G).[61]

To analyze the crystallographic structure of the exfoliated MPhene nanosheets, we performed X-ray diffraction (XRD). The experimental diffraction pattern of MPhene closely matched the simulated pattern based on our previously reported Bi-EA mesocrystal model (Table S3), confirming that exfoliation preserved the long-range molecular order (Fig. 2H). In contrast to the highly crystalline bulk Bi-EA mesocrystals, MPhene exhibits markedly reduced diffraction intensity, particularly for the reflection at approximately $2\theta \approx 10°$ associated with interlayer stacking (Fig. S10). The pronounced attenuation of this peak after exfoliation indicates a substantial reduction in interlayer stacking order and periodicity, consistent with the structural transformation from the bulk stacked material to ultrathin nanosheets.[62,63] High-resolution transmission electron microscopy (HRTEM) revealed well-defined lattice fringes with a periodic spacing of 0.34 nm throughout the nanosheet domain, closely matching the spacing of 0.36 nm predicted for π–π stacked EA ligands in our model (Fig. 2I and S11). Additionally, selected-area electron diffraction (SAED) patterns exhibited sharp, discrete diffraction spots, indicative of a high degree of crystallinity and in-plane ordering across the nanosheets (Fig. 2J). Furthermore, the measured d-spacing of the (2–10) crystallographic plane aligns with the simulated π–π stacking arrangement, forming a unique electron channel with a width of 0.70 nm, which highlights its nanoscale architecture that promotes highly efficient unidirectional electron transport (Fig. 2K).

To elucidate the electronic properties of MPhene, electron density calculations were performed along its in-plane structure using density functional theory (DFT) (Fig. 2L). The calculated electron density along the π–π stacking region was markedly higher than that in the non-stacked region (Fig. 2M). Furthermore, the electron density profile from a to b revealed significantly higher values in the π–π stacked EA molecules (6.49 e $Å^{-3}$) compared to the NMP molecules (0.13 e $Å^{-3}$), highlighting their role as preferential channels for highly efficient unidirectional electron transport (Fig. 2N). To experimentally validate these theoretical findings, we employed conductive atomic force microscopy (CAFM), a technique widely used to probe local electronic behaviors in 2D materials,[64] to directly visualize the electron transport channels within MPhene (Fig. 2O). The CAFM current patterns revealed channel-aligned bright stripes separated by darker regions, corresponding to parallel electron transport channels (Fig. 2P). Moreover, the line-scan current profile from c to d exhibited periodic peaks and troughs, corresponding respectively to channel and non-channel regions, in excellent agreement with the electron density distribution. The average peak current of the channel regions (9.1 nA) was substantially higher than that of the non-channel regions (0.2 nA), yielding a selectivity of $\sim$4500% (Fig. 2Q). These combined theoretical and experimental results unequivocally demonstrate the presence of unique unidirectional electron transport channels within MPhene.

Electrocatalytic performance of MPhene

To evaluate the role of unique π-stacking electron channels in facilitating highly efficient electron transport and enhancing the electrocatalytic activity of Bi^{III} active sites in MPhene, we carried out electrocatalytic CO_2RR measurements. Given the electron transport-dependent nature of CO_2RR, previously reported 2D nanomaterials were employed as benchmarks for comparative evaluation.[65] The CO_2RR activity of MPhene nanosheets was assessed in a three-electrode flow cell system using a CO_2-saturated $KHCO_3$ aqueous solution as the electrolyte (Fig. 3A and B). Linear sweep voltammetry (LSV) was performed within the potential range of 0 to -1.1 V (*vs.* RHE; all potentials mentioned in the following are referenced to RHE unless otherwise stated). MPhene exhibited a high current density (126 mA cm^{-2} at -1.1 V), indicating the considerable electron transport efficiency and high CO_2RR activity (Fig. 3C). From the chronoamperometric curves, the current density was consistent with the LSV curves and remained steady, suggesting the reliable electrocatalytic stability of MPhene (Fig. 3D).

Additionally, the electrocatalytic selectivity of MPhene nanosheets was verified by monitoring the products formed at each potential with ^1H nuclear magnetic resonance (^1H NMR) and mass spectrometry. The results revealed that HCOOH emerged as the primary product (Fig. 3E, F, S12 and S13). MPhene showed high selectivity towards HCOOH production, with the Faradaic efficiency of HCOOH (FE_{HCOOH}) exceeding 90% in a relatively wide potential window from -0.7 to -1.1 V.

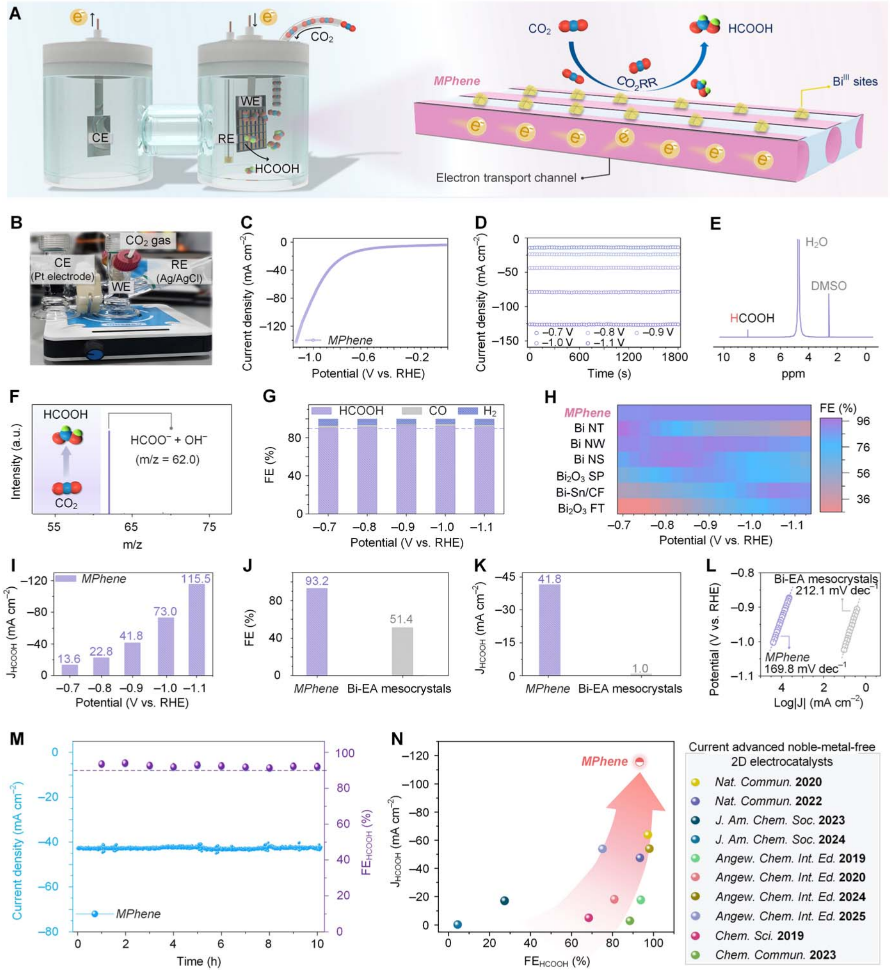

Fig. 3 Electrocatalytic performance of MPhene. (A) Schematic illustration of unique electron transport channels from MPhene for highly efficient electrocatalysis of CO_2 (right) with a three-electrode flow cell system (left). (B) Digital image of a three-electrode flow cell system for electrocatalysis of CO_2. (C and D) LSV curve (C) and chronoamperometric curves (D) of MPhene. (E and F) ^{1}H NMR spectra (E) and mass spectra (F) of the liquid product during the electrocatalysis of CO_2. (G) Faradaic efficiencies of HCOOH, CO, and H_2 for MPhene. (H) Comparison of the Faradaic efficiency of HCOOH between the reported Bi-based electrocatalysts and the current MPhene at different potentials. (I) Partial current density of HCOOH for MPhene. (J and K) Faradaic efficiency (J) and partial current density (K) of HCOOH for MPhene and Bi-EA mesocrystals at a potential of −0.9 V *vs.* RHE. (L) Tafel slope of MPhene and Bi-EA mesocrystals. (M) Electrocatalytic stability and selectivity of MPhene at a potential of −0.9 V *vs.* RHE for 10 h. (N) Comparison of the Faradaic efficiency and partial current density of HCOOH with reported electrocatalysts from nanosheets in neutral electrolytes.

The maximum value of FE_{HCOOH} reached 93.2% at −0.9 V (Fig. 3G), surpassing most of the other state-of-the-art Bi-based materials (Fig. 3H).[66–71] The calculated HCOOH partial current density (J_{HCOOH}) of MPhene reached a maximum value of 115.5 mA cm^{-2} at −1.1 V (Fig. 3I), highlighting its remarkable HCOOH-generating efficiency. In contrast, the unexfoliated Bi-EA mesocrystals exhibited considerably lower current density (<10 mA cm^{-2} at −1.1 V) and FE_{HCOOH} (<52%), as well as larger Tafel slope (212.1 mV dec^{-1}), resulting in minimal efficiency (J_{HCOOH} < 3 mA cm^{-2} from −0.7 to −1.1 V) (Fig. 3J–L and S14–S17) due to their poor conductivity. To further distinguish the contribution of increased surface area from the intrinsic catalytic properties of the materials, a surface-area-normalized analysis was carried out based on the electrochemical surface area (ECSA) measurements of the catalysts (Fig. S18). The normalized partial current densities for formate production are 0.12 mA cm^{-2} for the mesocrystals and 0.78 mA cm^{-2} for MPhene nanosheets, which still exhibit approximately 6.5-fold higher activity after normalization. Additionally, the turnover frequency (TOF) values for formate production increase from 0.02 s^{-1} for the mesocrystals to 0.90 s^{-1} for MPhene nanosheets. These results indicate that the enhanced catalytic performance of MPhene is not solely attributable to the increase in exposed surface area but instead reflects improved intrinsic catalytic properties together with more efficient charge transport within the MPhene structure.

The long-term electrocatalytic stability and product selectivity of MPhene were further evaluated. The total current density stabilized at ∼43 mA cm^{-2} together with an average FE_{HCOOH} of ∼92% over 10 h (Fig. 3M), indicating good catalytic stability and selectivity during the tested period. However, upon extending the electrolysis duration beyond 10 h, the current

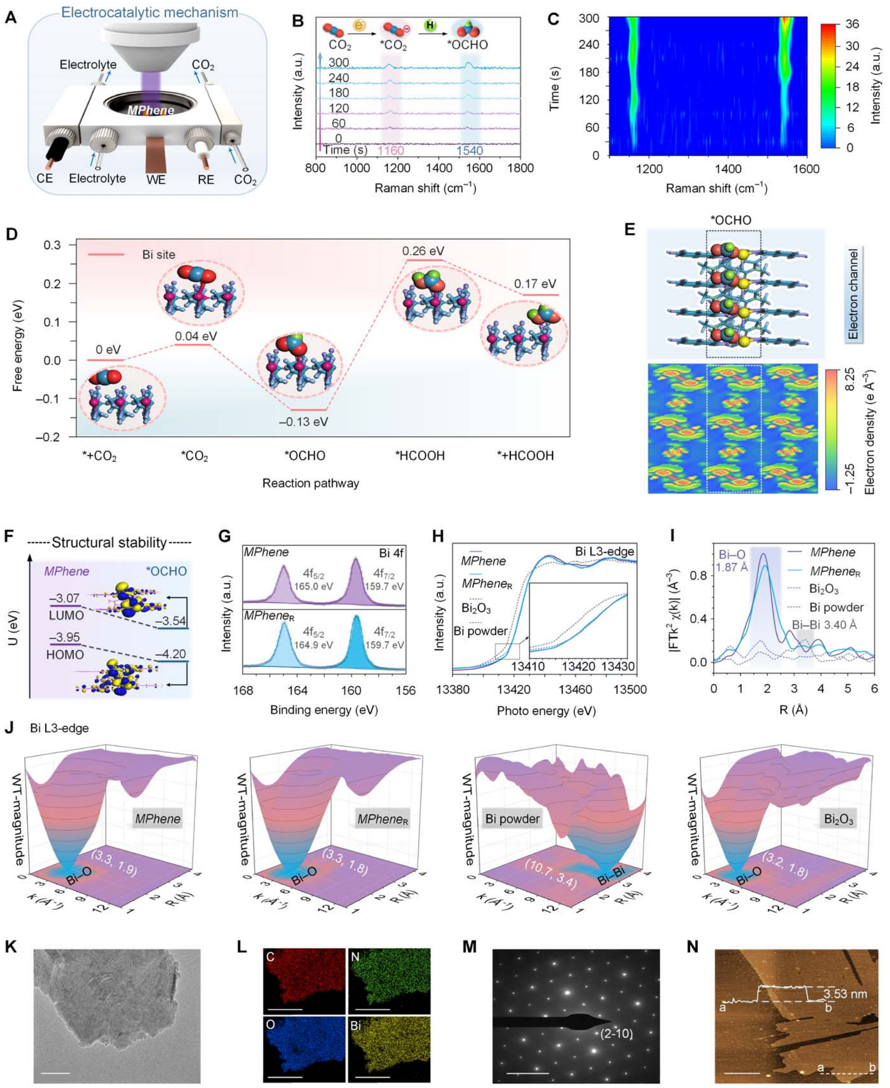

Fig. 4 Mechanistic studies and stability of MPhene during the CO_2RR process. (A) Schematic illustration of the *in situ* Raman device during the CO_2RR process. (B and C) Time-resolved *in situ* Raman spectra of MPhene in 0.5 M $KHCO_3$ solution under CO_2 bubbling. (D) Free energy diagrams of the electroreduction of CO_2 to HCOOH by MPhene. (E) Structure (top) and corresponding electron density (bottom) of the *OCHO intermediate. (F) The energy level and orbital diagram of HOMO and LUMO for MPhene and the *OCHO intermediate. (G) XPS spectra of Bi 4f for MPhene before and after CO_2RR. (H and I) Bi L3-edge XANES spectra (H) and FT-EXAFS spectra (I) of MPhene before and after CO_2RR. (J) Wavelet transform of the k^2-weighted EXAFS data of Bi L3-edge. (K–N) TEM image: (K), EDS elemental mapping images (L), SAED pattern (M), and AFM image (N) of MPhene after CO_2RR. Scale bars are 1 μm (K and N), 500 nm (L), and 5 1/nm (M).

density showed a noticeable decline at 16 h and further decayed during prolonged operation, reaching approximately 50% of its initial value by 30 h (Fig. S19). Post-reaction HRTEM and SAED analyses after extended electrolysis revealed structural changes in MPhene, including lattice fringes assignable to metallic Bi and diminished diffraction order of the supramolecular framework (Fig. S20), suggesting that the performance loss is associated with both partial reduction of Bi^{III} species and structural disordering under prolonged electrochemical conditions. A comparative analysis of overall CO_2RR performance based on FE_{HCOOH} and J_{HCOOH} values demonstrates that MPhene nanosheets achieve record-high electrocatalytic activity in neutral electrolytes, far exceeding the state-of-the-art performance of noble-metal-free 2D electrocatalysts (Fig. 3N and Table S4). These results highlight the superiority of unique long-range π-stacking channels for highly efficient electron transport during electrocatalysis.

Electrocatalytic mechanism and stability of MPhene

In situ electrochemical Raman spectroscopy was employed to elucidate the role of unique π-stacking electron channels of MPhene during the CO_2RR, tracking intermediate species and the reaction kinetics (Fig. 4A). The characteristic peaks centered at 1160 and 1540 cm^{-1} were detected and gradually increased over time (Fig. 4B and C), corresponding to the generation of surface-adsorbed carbonate species (*CO_2) and proton-trapped carboxylate radicals (*OCHO).[53] We further calculated the Gibbs free energies of all intermediates at actual work conditions

(0.5 M $KHCO_3$) to analyze the entire reaction pathway in detail. The results exhibited a lower thermodynamic energy barrier in the formation of *OCHO on the Bi site than other intermediates (Fig. 4D), which is consistent with the Brønsted–Evans–Polanyi (BEP) relationship,[72] indicating the crucial role of MPhene in the activation of CO_2 molecules to form the *OCHO intermediate.

DFT calculations were further used to analyze the electron density of MPhene during the formation of the *OCHO intermediate. It was revealed that the *OCHO intermediate had strong electron density along the electron channels (Fig. 4E), revealing the vital role of unique long-range π-stacking channels in promoting electron transport of the *OCHO intermediate. Density of states (DOS) analysis of the *OCHO intermediate showed a narrower bandwidth (1.09 eV) compared with pristine MPhene (1.20 eV), illustrating the improved conductivity responsible for the effective transformation of the *OCHO intermediate during the CO_2RR process. Furthermore, the contribution to the total DOS for the *OCHO intermediate, situated beneath the Fermi level, stems from the bonding hybridization of C p and Bi p states within the unique π-stacking electron channels, fundamentally strengthening its conductive nature (Fig. S21). The electronic overlap and the decreased energy levels of the highest occupied molecular orbital (HOMO) and lowest unoccupied molecular orbital (LUMO) for the *OCHO intermediate further confirm the enhanced conductivity during the CO_2RR process (Fig. 4F). Collectively, these findings demonstrate that electrons transfer from Bi^{III} catalytic sites embedded in the unique electron channels to adsorbed CO_2 molecules, leading to the generation of a stable and conductive *OCHO intermediate and subsequent HCOOH formation (Fig. S22).

Owing to the efficient charge transport enabled by the long-range π-stacking channels, MPhene exhibits improved structural robustness during the initial CO_2RR process, thereby mitigating the rapid reduction and collapse often observed in coordinated metal-based materials.[73,74] In XPS spectra, the Bi 4f core-level signals of pristine MPhene and MPhene after the 10 h CO_2RR test ($MPhene_R$) remained largely comparable, suggesting that the Bi^{III}-coordinated environment was largely retained during the initial electrolysis period (Fig. 4G). To further elucidate the coordination environment of Bi^{III} active sites, XAFS spectroscopy was conducted. In the Bi L3-edge X-ray absorption near-edge structure (XANES) spectra, the absorption edge and the white line peak of the XANES spectrum in $MPhene_R$ nearly coincided with those observed for the Bi_2O_3 reference, indicating that the Bi^{III} species were largely retained after the 10 h CO_2RR test (Fig. 4H). Moreover, FT-EXAFS spectra were analyzed to discern the atomic-scale local environment of the Bi^{III} sites. The prominent peak in the $MPhene_R$ spectrum resided at 1.87 Å, consistent with the pristine MPhene (Fig. 4I), suggesting that the local coordination structure was largely preserved during the initial electrolysis period. Complementary wavelet transform (WT) analysis of the Bi L3-edge EXAFS oscillations supported this finding. The WT contour maps of $MPhene_R$ exhibited a solitary intensity maximum centered around 1.80 Å, corresponding to the Bi–O coordination within the MPhene nanosheets, as opposed to the metallic Bi–Bi bonding (3.40 Å) characteristic of Bi powders (Fig. 4J).

Simultaneously, TEM and EDS mapping observations revealed the intact structure of $MPhene_R$ with sheet-like morphologies and uniform distributions of each element in $MPhene_R$ (Fig. 4K and L). In addition, the distinct diffraction pattern of SAED for $MPhene_R$ further strengthens the results of XPS and XAFS (Fig. 4M). The measured thickness of $MPhene_R$ was 3.53 nm (Fig. 4N), which was nearly the same as MPhene, indicating the absence of reassembly of nanosheets during electroreduction. In contrast, the XPS spectra, SEM, and TEM images of Bi-EA mesocrystals changed dramatically after CO_2RR (Fig. S23–S25). In summary, all analyses consistently confirmed that the highly active Bi oxidation state and structure within MPhene can be stabilized owing to the unidirectional and ultrafast electron transport ability, as well as the subsequent absence of accumulation of electrons from unique long-range π-stacking channels,[75] demonstrating the advantages of MPhene in electrocatalytic research and applications.

Conclusions

Unidirectional electron transport channels were successfully established through the formation of unique extended π-stacking architectures within 2D metal–organic nanosheets (MPhene). These nanosheets exhibit unidirectional and highly efficient electron transport to Bi^{III} active sites, effectively minimizing energy dissipation and enhancing the accessibility of catalytic centers. Consequently, MPhene nanosheets exhibit outstanding electrocatalytic selectivity, achieving a formic acid Faradaic efficiency exceeding 90% within a broad potential window (−0.7 to −1.1 V *vs.* RHE). Moreover, the partial current density for formic acid production reached 115.5 mA cm^{-2} at −1.1 V *vs.* RHE, establishing record-high electrocatalytic activity among all previously reported advanced noble-metal-free 2D electrocatalysts in neutral electrolytes. This work further demonstrates a sustainable, noble-metal-free strategy that rivals the efficiency of noble-metal systems, highlighting its potential for scalable and eco-friendly CO_2 conversion. *In situ* Raman spectroscopy and DFT calculations indicated that the unique π-stacking electron channels in MPhene exhibited highly efficient unidirectional electron transport properties, accounting for the highly selective and effective electroreduction of CO_2 to formic acid. Benefiting from the nanoscale electron transport channels, the coordinated Bi species were retained, thereby driving the electroreduction of CO_2 molecules during the CO_2RR process. Collectively, these findings establish a distinctive paradigm for engineering unique unidirectional electron transport channels in 2D electrocatalysts and delineate a promising route toward advanced electrochemical technologies, with broad implications for carbon-neutral energy conversion and environmental remediation.

Author contributions

Y. H., G. H., W. L., I. M., and J. G. conceived the ideas. Q. X. and G. H. conducted material design and synthesis. Q. X. and G. H.

performed theoretical calculations. Q. X., Y. H., Q. L., S. D., and X. W. conceived the electrocatalytic experiments and performed the corresponding data analysis. Q. X., G. H., W. L., and J. G. drafted the manuscript. All authors discussed the results and commented on the manuscript.

Conflicts of interest

J. G. and Y. H. are equity holders of Novastra Therapeutics. J. G. is a shareholder and board director of Vitagenix Bio. All other authors declare no competing interests.

Data availability

The data supporting this article have been included as part of the supplementary information (SI). Supplementary information: experimental section, synthetic procedures, and characterization data (including electrochemical measurements and *in situ* Raman spectroscopy) for metal–organic nanosheets; structural details and electrocatalytic CO_2 reduction properties; as well as structural stability analyses. See DOI: https://doi.org/10.1039/d5sc09348a.

Acknowledgements

The authors would like to dedicate this article to Prof. Ian Manners. His dedication to science, family, and life will forever be cherished. His immense scientific legacy will eternally be remembered, and the remaining authors are profoundly grateful for the invaluable guidance he imparted during the collaborative journey. The authors would also like to express their sincere gratitude to Deborah O'Hanlon-Manners for her helpful discussion and heartwarming support. The authors would like to thank Z. Wang, Q. Song, and M. Zhou at the College of Biomass Science and Engineering of Sichuan University for characterization assistance. The authors also appreciate S. Wang from the Analytical and Testing Center of Sichuan University for help with the transmission electron microscope characterizations. Funding: The authors acknowledge financial support from the National Key R&D Program of China (2022YFA0912800), the National Excellent Young Scientists Fund (00308054A1045), the National Natural Science Foundation of China (22178233, 22408241, 22108181), the Talents Program of Sichuan Province, the Fundamental Research Funds for the Central Universities (SCU2025D014), the Double First-Class University Plan of Sichuan University, the State Key Laboratory of Polymer Materials Engineering (sklpme 2020-03-01), the Tianfu Emei Program of Sichuan Province (2022-EC02-00073-CG), the Postdoctoral special funding of Sichuan Province (TB2022063), China Postdoctoral Science Foundation (2023M742459), Ministry of Education Key Laboratory of Leather Chemistry and Engineering, and National Engineering Research Center of Clean Technology in Leather Industry.

References

1 D. Shindell and C. J. Smith, *Nature*, 2019, **573**, 408–411.
2 Z. Liu, Z. Deng, S. J. Davis and P. Ciais, *Nat. Rev. Earth Environ.*, 2024, **5**, 253–254.
3 M. Kotz, A. Levermann and L. Wenz, *Nature*, 2024, **628**, 551–557.
4 A. Stechemesser, N. Koch, E. Mark, E. Dilger, P. Klösel, L. Menicacci, D. Nachtigall, F. Pretis, N. Ritter, M. Schwarz, H. Vossen and A. Wenzel, *Science*, 2024, **385**, 884–892.
5 Y. Y. Birdja, E. Pérez-Gallent, M. C. Figueiredo, A. J. Göttle, F. Calle-Vallejo and M. T. M. Koper, *Nat. Energy*, 2019, **4**, 732–745.
6 H. Wang, Y.-K. Tzeng, Y. Ji, Y. Li, J. Li, X. Zheng, A. Yang, Y. Liu, Y. Gong, L. Cai, Y. Li, X. Zhang, W. Chen, B. Liu, H. Lu, N. A. Melosh, Z.-X. Shen, K. Chan, T. Tan, S. Chu and Y. Cui, *Nat. Nanotechnol.*, 2020, **15**, 131–137.
7 J. L. Hitt, Y. C. Li, S. Tao, Z. Yan, Y. Gao, S. J. L. Billinge and T. E. Mallouk, *Nat. Commun.*, 2021, **12**, 1114.
8 A. M. Alfaraidi, B. Kudisch, N. Ni, J. Thomas, T. Y. George, K. Rajabimoghadam, H. J. Jiang, D. G. Nocera, M. J. Aziz and R. Y. Liu, *J. Am. Chem. Soc.*, 2023, **145**, 26720–26727.
9 Y. Yang, S. Louisia, S. Yu, J. Jin, I. Roh, C. Chen, M. V. Fonseca Guzman, J. Feijóo, P.-C. Chen, H. Wang, C. J. Pollock, X. Huang, Y.-T. Shao, C. Wang, D. A. Muller, H. D. Abruña and P. Yang, *Nature*, 2023, **614**, 262–269.
10 S. J. Cobb, S. Rodríguez-Jiménez and E. Reisner, *Angew. Chem., Int. Ed.*, 2024, **63**, e202310547.
11 L. Fan, F. Li, T. Liu, J. E. Huang, R. K. Miao, Y. Yan, S. Feng, C.-W. Tai, S.-F. Hung, H.-J. Tsai, M.-C. Chen, Y. Bai, D. Kim, S. Park, P. Papangelakis, C. Wu, A. Shayesteh Zeraati, R. Dorakhan, L. Sun, D. Sinton and E. Sargent, *Nat. Synth.*, 2025, **4**, 262–270.
12 A. C. Hartnett, R. J. Evenson, A. E. Thorarinsdottir, S. S. Veroneau and D. G. Nocera, *J. Am. Chem. Soc.*, 2025, **147**, 1123–1133.
13 S. Navarro-Jaén, M. Virginie, J. Bonin, M. Robert, R. Wojcieszak and A. Y. Khodakov, *Nat. Rev. Chem.*, 2021, **5**, 564–579.
14 Z. W. Seh, J. Kibsgaard, C. F. Dickens, I. Chorkendorff, J. K. Nørskov and T. F. Jaramillo, *Science*, 2017, **355**, eaad4998.
15 X. Chia and M. Pumera, *Nat. Catal.*, 2018, **1**, 909–921.
16 M. A. Topinka, B. J. LeRoy, R. M. Westervelt, S. E. J. Shaw, R. Fleischmann, E. J. Heller, K. D. Maranowski and A. C. Gossard, *Nature*, 2001, **410**, 183–186.
17 Z. J. Krebs, W. A. Behn, S. Li, K. J. Smith, K. Watanabe, T. Taniguchi, A. Levchenko and V. W. Brar, *Science*, 2023, **379**, 671–676.
18 G. Varnavides, A. Yacoby, C. Felser and P. Narang, *Nat. Rev. Mater.*, 2023, **8**, 726–741.
19 J. Xie, J. Zhang, S. Li, F. Grote, X. Zhang, H. Zhang, R. Wang, Y. Lei, B. Pan and Y. Xie, *J. Am. Chem. Soc.*, 2013, **135**, 17881–17888.
20 H. Zhang, L. Wu, R. Feng, S. Wang, C.-S. Hsu, Y. Ni, A. Ahmad, C. Zhang, H. Wu, H.-M. Chen, W. Zhang, Y. Li, P. Liu and F. Song, *ACS Catal.*, 2023, **13**, 6000–6012.
21 W. Li, Y. Liu, A. Azam, Y. Liu, J. Yang, D. Wang, C. C. Sorrell, C. Zhao and S. Li, *Adv. Mater.*, 2024, **36**, 2404658.

22 Y. Sun, S. Gao, F. Lei and Y. Xie, *Chem. Soc. Rev.*, 2015, **44**, 623–636.

23 Y. Gao, H. Liang, H. Xu, D. Cui, C. Wu, J. Chen, Y. Liu, S.-x. Dou, W. Huang and L. Lin, *ACS Energy Lett.*, 2024, **9**, 3982–4002.

24 G. Skorupskii, B. A. Trump, T. W. Kasel, C. M. Brown, C. H. Hendon and M. Dincă, *Nat. Chem.*, 2020, **12**, 131–136.

25 J. Yi, G. Zhang, H. Yu and H. Yan, *Nat. Rev. Mater.*, 2023, **9**, 46–62.

26 L. Han, M. Wang, X. Jia, W. Chen, H. Qian and F. He, *Nat. Commun.*, 2018, **9**, 865.

27 Z. Liu, Y. Xie, L. Liu, X. Cai, H. Q. Yin, M. Zuo, Y. Liu, S. Feng, W. Huang and D. Wu, *Small*, 2023, **20**, 2309194.

28 J. Guo, Y. Ping, H. Ejima, K. Alt, M. Meissner, J. J. Richardson, Y. Yan, K. Peter, D. von Elverfeldt, C. E. Hagemeyer and F. Caruso, *Angew. Chem., Int. Ed.*, 2014, **53**, 5546–5551.

29 J. Guo, B. L. Tardy, A. J. Christofferson, Y. Dai, J. J. Richardson, W. Zhu, M. Hu, Y. Ju, J. Cui, R. R. Dagastine, I. Yarovsky and F. Caruso, *Nat. Nanotechnol.*, 2016, **11**, 1105–1111.

30 J. Guo, M. Suástegui, K. K. Sakimoto, V. M. Moody, G. Xiao, D. G. Nocera and N. S. Joshi, *Science*, 2018, **362**, 813–816.

31 X. Qiu, X. Wang, Y. He, J. Liang, K. Liang, B. L. Tardy, J. J. Richardson, M. Hu, H. Wu, Y. Zhang, O. J. Rojas, I. Manners and J. Guo, *Sci. Adv.*, 2021, **7**, eabh3482.

32 Y. He, Y. Tang, Y. Zhang, L. MacFarlane, J. Shang, H. Shi, Q. Xie, H. Zhao, I. Manners and J. Guo, *Appl. Phys. Rev.*, 2022, **9**, 021301.

33 J. Pan, G. Gong, Q. Wang, J. Shang, Y. He, C. Catania, D. Birnbaum, Y. Li, Z. Jia, Y. Zhang, N. S. Joshi and J. Guo, *Nat. Commun.*, 2022, **13**, 2117.

34 Y. Wang, Y. He, Q. Wang, X. Wang, B. L. Tardy, J. J. Richardson, O. J. Rojas and J. Guo, *Matter*, 2023, **6**, 260–273.

35 Y. Wang, M. Wang, Q. Wang, T. Wang, Z. Zhou, M. Mehling, T. Guo, H. Zou, X. Xiao, Y. He, X. Wang, O. J. Rojas and J. Guo, *Adv. Mater.*, 2023, **35**, 2301531.

36 C. Zhang, Y. Tang, Q. Wang, Y. He, X. Wang, S. Beyer and J. Guo, *Chin. Chem. Lett.*, 2023, **34**, 107795.

37 G. Lang, J. Feng, B. Feng, J. Hu, Z. Ran, Z. Zhou, Z. Jiang, Y. He and J. Guo, *Chin. Chem. Lett.*, 2024, **35**, 109113.

38 N. Pang, Y. He, M. Wang, X. Wang, J. Guo, X. Liao and B. Shi, *Chin. Chem. Lett.*, 2025, **36**, 110914.

39 Y. Wang, Y. He, G. Hong, X. Wang and J. Guo, *Sci. Sin. Chim.*, 2025, **55**, 37–49.

40 Y. Wu, Q. Ma, Q. Liu, M. Wang, W. Wei, G. Gong, Y. He, Y. Wang, Y. Zheng, L. Yang, G. Nyström and J. Guo, *Cell Biomater.*, 2025, **1**, 100019.

41 G. Giri, E. Verploegen, S. C. B. Mannsfeld, S. Atahan-Evrenk, D. H. Kim, S. Y. Lee, H. A. Becerril, A. Aspuru-Guzik, M. F. Toney and Z. Bao, *Nature*, 2011, **480**, 504–508.

42 P. A. Korevaar, S. J. George, A. J. Markvoort, M. M. J. Smulders, P. A. J. Hilbers, A. P. H. J. Schenning, T. F. A. De Greef and E. W. Meijer, *Nature*, 2012, **481**, 492–496.

43 S. Liu, X. F. Lu, J. Xiao, X. Wang and X. W. Lou, *Angew. Chem., Int. Ed.*, 2019, **58**, 13828–13833.

44 F. Yang, A. O. Elnabawy, R. Schimmenti, P. Song, J. Wang, Z. Peng, S. Yao, R. Deng, S. Song, Y. Lin, M. Mavrikakis and W. Xu, *Nat. Commun.*, 2020, **11**, 1088.

45 P. Wang, S. Meng, B. Zhang, M. He, P. Li, C. Yang, G. Li and Z. Li, *J. Am. Chem. Soc.*, 2023, **145**, 26133–26143.

46 X. He, Y. Guo, J. Zhang, S. Yang, J. Chen, S. Li, S. Xie, Y. Wang and C. Wang, *Chem. Commun.*, 2023, **59**, 5737–5740.

47 S.-Z. Hou, X.-D. Zhang, W.-W. Yuan, Y.-X. Li and Z.-Y. Gu, *Inorg. Chem.*, 2020, **59**, 11298–11304.

48 D. Yang, S. Zuo, H. Yang, Y. Zhou and X. Wang, *Angew. Chem., Int. Ed.*, 2020, **59**, 18954–18959.

49 J.-X. Wu, S.-Z. Hou, X.-D. Zhang, M. Xu, H.-F. Yang, P.-S. Cao and Z.-Y. Gu, *Chem. Sci.*, 2019, **10**, 2199–2205.

50 X. Chen, S. Lv, H. Gu, H. Cui, G. Liu, Y. Liu, Z. Li, Z. Xu, J. Kang, G. Teobaldi, L.-M. Liu and L. Guo, *J. Am. Chem. Soc.*, 2024, **146**, 13527–13535.

51 H. Liu, Y. Bai, M. Wu, Y. Yang, Y. Wang, L. Li, J. Hao, W. Yan and W. Shi, *Angew. Chem., Int. Ed.*, 2024, **63**, e202411575.

52 M. Zhang, W. Zhu, Z. Liu, S. Chen, D. Zhou, X. Mu, Z. Zhuang, S. Wang, J. Yang, Y. Du, X. Luo, Q. Zhang, S. Liu, D. Wang and Z. Dai, *Angew. Chem., Int. Ed.*, 2025, **64**, e202510206.

53 J. Duan, T. Liu, Y. Zhao, R. Yang, Y. Zhao, W. Wang, Y. Liu, H. Li, Y. Li and T. Zhai, *Nat. Commun.*, 2022, **13**, 2039.

54 V. Nicolosi, M. Chhowalla, M. G. Kanatzidis, M. S. Strano and J. N. Coleman, *Science*, 2013, **340**, 1226419.

55 A. Puthirath Balan, S. Radhakrishnan, C. F. Woellner, S. K. Sinha, L. Deng, C. d. l. Reyes, B. M. Rao, M. Paulose, R. Neupane, A. Apte, V. Kochat, R. Vajtai, A. R. Harutyunyan, C.-W. Chu, G. Costin, D. S. Galvao, A. A. Martí, P. A. van Aken, O. K. Varghese, C. S. Tiwary, A. Malie Madom Ramaswamy Iyer and P. M. Ajayan, *Nat. Nanotechnol.*, 2018, **13**, 602–609.

56 R. Dong and X. Feng, *Nat. Mater.*, 2021, **20**, 122–123.

57 J. N. Coleman, M. Lotya, A. O'Neill, S. D. Bergin, P. J. King, U. Khan, K. Young, A. Gaucher, S. De, R. J. Smith, I. V. Shvets, S. K. Arora, G. Stanton, H. Y. Kim, K. Lee, G. T. Kim, G. S. Duesberg, T. Hallam, J. J. Boland, J. J. Wang, J. F. Donegan, J. C. Grunlan, G. Moriarty, A. Shmeliov, R. J. Nicholls, J. M. Perkins, E. M. Grieveson, K. Theuwissen, D. W. McComb, P. D. Nellist and V. Nicolosi, *Science*, 2011, **331**, 568–571.

58 C. Zhu, X. Zhang, Y. Li, L. Chen, Y. Sun, X. Li, J. Zhang, J. Liu, X. Li, Y. Wu, H. Wang, F. Wang, L. Zhang and H. Guo, *Adv. Mater.*, 2020, **32**, 1906539.

59 Q. Li, Y. Wang, X. Xiao, R. Zhong, J. Liao, J. Guo, X. Liao and B. Shi, *J. Hazard. Mater.*, 2020, **398**, 122943.

60 W. Xu, H. Wang, Y. Tao and X. Zheng, *J. Raman Spectrosc.*, 2017, **49**, 362–371.

61 C. F. Wang, R. F. Li, X. Y. Chen, R. J. Wei, L. S. Zheng and J. Tao, *Angew. Chem., Int. Ed.*, 2014, **54**, 1574–1577.

62 W. M. Liao, J. H. Zhang, S. Y. Yin, H. Lin, X. M. Zhang, J. H. Wang, H. P. Wang, K. Wu, Z. Wang, Y. N. Fan, M. Pan and C. Y. Su, *Nat. Commun.*, 2018, **9**, 2401.

63 T. Sun, S. Li, L. Zhang and Y. Xu, *Angew. Chem., Int. Ed.*, 2023, **62**, e202301865.

64 Z. Wei, D. Wang, S. Kim, S.-Y. Kim, Y. Hu, M. K. Yakes, A. R. Laracuente, Z. Dai, S. R. Marder, C. Berger, W. P. King, W. A. de Heer, P. E. Sheehan and E. Riedo, *Science*, 2010, **328**, 1373–1376.

65 K. L. Zhou, Z. Wang, C. B. Han, X. Ke, C. Wang, Y. Jin, Q. Zhang, J. Liu, H. Wang and H. Yan, *Nat. Commun.*, 2021, **12**, 3783.

66 N. Han, Y. Wang, H. Yang, J. Deng, J. Wu, Y. Li and Y. Li, *Nat. Commun.*, 2018, **9**, 1320.

67 G. Wen, D. U. Lee, B. Ren, F. M. Hassan, G. Jiang, Z. P. Cano, J. Gostick, E. Croiset, Z. Bai, L. Yang and Z. Chen, *Adv. Energy Mater.*, 2018, **8**, 1802427.

68 P. Deng, H. Wang, R. Qi, J. Zhu, S. Chen, F. Yang, L. Zhou, K. Qi, H. Liu and B. Y. Xia, *ACS Catal.*, 2019, **10**, 743–750.

69 Q. Gong, P. Ding, M. Xu, X. Zhu, M. Wang, J. Deng, Q. Ma, N. Han, Y. Zhu, J. Lu, Z. Feng, Y. Li, W. Zhou and Y. Li, *Nat. Commun.*, 2019, **10**, 2807.

70 T. Tran-Phu, R. Daiyan, Z. Fusco, Z. Ma, R. Amal and A. Tricoli, *Adv. Funct. Mater.*, 2019, **30**, 1906478.

71 X. Zhang, X. Sun, S.-X. Guo, A. M. Bond and J. Zhang, *Energy Environ. Sci.*, 2019, **12**, 1334–1340.

72 J. Yang, X. Wang, Y. Qu, X. Wang, H. Huo, Q. Fan, J. Wang, L. M. Yang and Y. Wu, *Adv. Energy Mater.*, 2020, **10**, 2001709.

73 F. Lei, W. Liu, Y. Sun, J. Xu, K. Liu, L. Liang, T. Yao, B. Pan, S. Wei and Y. Xie, *Nat. Commun.*, 2016, **7**, 12697.

74 D.-H. Nam, O. S. Bushuyev, J. Li, P. De Luna, A. Seifitokaldani, C.-T. Dinh, F. P. García de Arquer, Y. Wang, Z. Liang, A. H. Proppe, C. S. Tan, P. Todorović, O. Shekhah, C. M. Gabardo, J. W. Jo, J. Choi, M.-J. Choi, S.-W. Baek, J. Kim, D. Sinton, S. O. Kelley, M. Eddaoudi and E. H. Sargent, *J. Am. Chem. Soc.*, 2018, **140**, 11378–11386.

75 F. Li, X. V. Medvedeva, J. J. Medvedev, E. Khairullina, H. Engelhardt, S. Chandrasekar, Y. Guo, J. Jin, A. Lee, H. Thérien-Aubin, A. Ahmed, Y. Pang and A. Klinkova, *Nat. Catal.*, 2021, **4**, 479–487.